





Interfacial ion-electron conversion enhanced moisture energy harvester

Received: 23 October 2024

Accepted: 4 July 2025

Published online: 17 July 2025

Puying Li ^{1,2}, Yajie Hu ^{1,2}, Haiyan Wang^{1,2}, Tiancheng He^{1,2,3}, Huhu Cheng ^{1,2} & Liangti Qu ^{1,2} ✉

Harvesting energy from the surrounding environment holds great promise for meeting decentralized energy demands and facilitating the transition to a low-carbon economy. Ubiquitous moisture in the air offers a natural energy reservoir, but very little has yet been harnessed. Conventional moisture-electricity generators collect moisture energy through the directional migration of ions in the moisture-sorption functional materials induced by a moisture field. However, the unsatisfactory output performance severely limits their practical implementation. Herein, we develop an ion-electron conversion enhanced moisture energy harvester (*i*-eMEH) by creating an ion-enriched storage interface and concurrently inducing a faradic process through the dual redox couples in the functional layer/electrode interfaces. The *i*-eMEH reaches a record-high peak current of 9.2 mA cm⁻² and power density of 6.7 W m⁻², ~60 times higher than those of reported moisture-electricity generators, and approaching the output level of perovskite solar cells and thermoelectric devices. The output rises to hundreds of milliamperes and tens of volts through the device enlargement and integration, thus efficiently charging the capacitor (4F) and commercial lithium battery. This moisture energy harvester manifests the great potential for miniaturized flexible electronics and presents a crucial step towards practical applications of moisture energy harvest.

Green energy harvesting technologies significantly alleviate the energy crisis and reduce greenhouse gas emissions^{1–7}. Ubiquitous gaseous moisture in the atmosphere, as a natural energy reservoir, is promising for developing new types of power-generating systems despite the lack of sufficient research and utilization so far^{1,8}. Moisture energy is embodied in the conversion of water between the high-enthalpy high-entropy gaseous state and the low-enthalpy low-entropy adsorbed state, with enthalpy variation of ~2500 kJ kg_{water}⁻¹ and entropy variation ~8 kJ kg_{water}⁻¹ K⁻¹, sufficiently satisfying the decentralized energy demands^{1,8,9}. Therefore, moisture-enabled electrical generation by utilization of moisture energy has been brought to the forefront of

researchers' attention since first implemented experimentally in 2015^{10–13}. For these moisture-electricity generators, the directional ion transport in the moisture-sorption functional layer under asymmetric moisture field induces the migration of electrons in the outer circuit, thus generating electricity (Supplementary Fig. 1a)^{10–13}. Up to now, the majority of studies have focused on the modification of functional layers to improve the water absorption capacity, increase migration ions quantity, and reduce ion migration resistance^{14–21}. However, these efforts have resulted in limited enhancement in electrical output (~100 mW m⁻², Supplementary Table 1), far lower than that of present green energy harvesting techniques, e.g., photovoltaics

¹State Key Laboratory of Flexible Electronics Technology, Ministry of Education, Department of Chemistry, Tsinghua University, Beijing, PR China. ²Key Laboratory of Organic Optoelectronics & Molecular Engineering, Ministry of Education, Department of Chemistry, Tsinghua University, Beijing, PR China.

³State Key Laboratory of Tribology in Advanced Equipment (SKLT), Department of Mechanical Engineering, Tsinghua University, Beijing, PR China.

✉ e-mail: lqu@tsinghua.edu.cn

(-120 W m^{-2})^{22–25}, thermoelectrics ($\sim 5 \text{ W m}^{-2}$)^{26–28}, severely restricting the practical application of moisture-electricity generators.

We have found that the inefficient ion-electron conversion between the functional layer and the electrode accounts for the low electrical output performance, which has yet garnered no attention to date. For the sake of chemical stability, inert electrodes are prevalently used as current collectors^{14,17,29,30}. However, it is reported that the ionic current cannot be effectively transformed into electronic signals at the functional layer/electrode interface due to the surge in interface impedance and electrode potential caused by the limited ion storage sites on the electrode surface (Fig. 1a)³¹. Simultaneously, a large internal electric field across the functional layer will be formed due to the increase in electrode potential, which will inhibit the directional migration of ions and induce the drift current counter to the diffusion current. The reverse migration of ions will diminish the induced charge on the electrode, leading to a decay in voltage (Supplementary Fig. 1a). Therefore, both the formation and attenuation of electrical generation are essentially associated with the ion-electron conversion at functional layer/electrode interface.

To address this issue, we herein develop an ion-electron conversion enhanced moisture energy harvester (*i*-eMEH). On the one hand, interface capacitance is increased through the introduction of

capacitive electrode materials. The increase in capacitance enables more ions to be stored on the interface, thereby improving peak current and voltage. Furthermore, the reduction in the built-in electric field weakens the decay rate of voltage and current (Fig. 1b)^{32–34}. On the other hand, a new ion-electron conversion route is created with the addition of redox couples in the functional layer/electrode interface. The electrons transferred between the redox couple and electrode also take part in the charge balance in the interface in the open-circuit state, realizing more ion storage on the electrode while stabilizing the electrode potential. These electrons will transfer in opposite direction to improve the electric generation when short-connected (Fig. 1c, Supplementary Fig. 1b and Supplementary Note 1). Therefore, the redox couples act as an “electron sponge” to promote ion-electron conversion. It is worth noting that the capacitive electrode materials and redox reactions mentioned above are different from the electrode consumption reaction in some MEGs^{35–37} and those with irreversible faradic reaction³⁸ (Supplementary Fig. 2 and Supplementary Note 2).

Results

Electrical generation performance of *i*-eMEHs

The *i*-eMEH is constructed from graphite foil, capacitive interface layers, and a functional layer (Fig. 2a, Methods). MoS₂ (Fig. 2b and

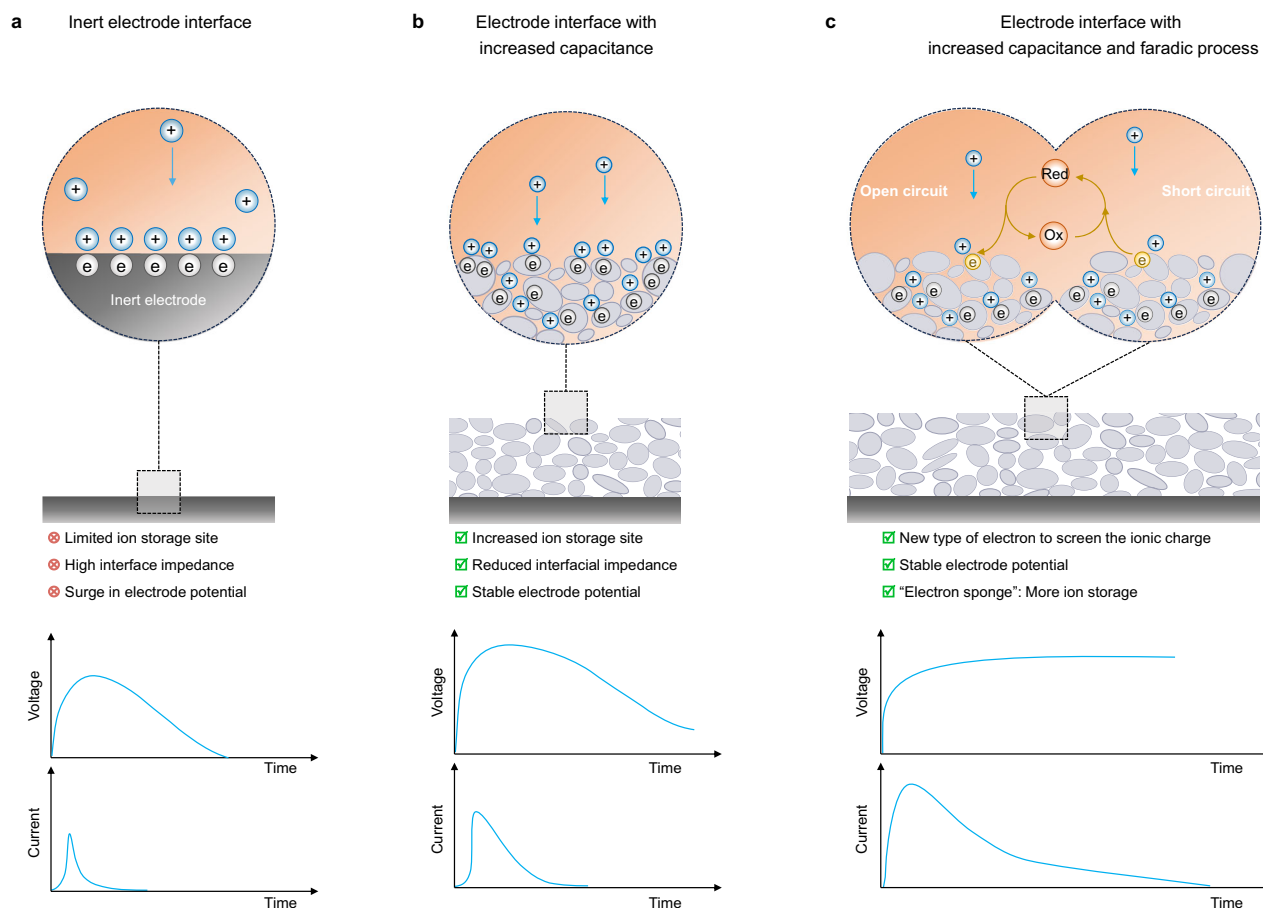


Fig. 1 | Designing strategies of ion-electron conversion enhanced moisture energy harvester (*i*-eMEH). **a** Schematic diagram of the electrode interface and the corresponding output performance of moisture-electricity generators with inert electrode. The insufficient ion storage on electrode will influence the ion-electron conversion at the interface, manifesting in low peak current. The formation of built-in electric field causes the rapid decay of voltage and current. **b** Schematic diagram of the electrode interface and the output performance of moisture-electricity generators with increased capacitance. The capacitive interface layer promotes the ion-electron conversion, bringing about the increase in peak current and voltage.

The restricted formation of built-in electric field weakens the decay rate of voltage and current. **c** Schematic diagram of the electrode interface and the output performance of *i*-eMEH with increased capacitance and faradic process. The introduction of redox couples at the interface creates a faradic process for further enhanced ion-electron conversion. The electron transferred in this way can also screen the ionic charge in the interface to stabilize the electrode potential and increase the amounts of ions stored on the electrode. The electron transfer will undergo opposite directions under open-circuit and short-circuit condition.

Supplementary Figs. 3a and 4a) and MnO_2 electrodes (Fig. 2c and Supplementary Figs. 3b and 4b) are used as the top and bottom electrodes of *i*-eMEH. Polystyrene sulfonic acid doped with sulfuric acid (PSS)³⁹ is used as the main functional layer modified with the redox couples of $\text{K}_3[\text{Fe}(\text{CN})_6]/\text{K}_4[\text{Fe}(\text{CN})_6]$ ($[\text{Fe}(\text{CN})_6]^{3/4-}$) and KI_3/KI (I_3^-/I^-) respectively on both sides (*rc*-PSS, Fig. 2d and Supplementary Figs. 5 and 7). Subsequently, the MoS_2 electrode, *rc*-PSS layer, and MnO_2 electrode are stacked layer by layer to form a sandwich-type *i*-eMEH. Typically, the *rc*-PSS layer is 1.48 mm thick, with redox couples decorated on both sides, each 370 μm thick, while the capacitive interface layer is 12 μm thick. The *i*-eMEH area is 1 cm \times 1 cm. For comparison, the moisture energy harvesters based on PSS sandwiched between graphite electrodes (MEH_g) and PSS sandwiched between MoS_2 electrode and MnO_2 electrode (MEH_M) are constructed, respectively.

The MEH_g generates a low open-circuit voltage (V_{OC}) of 0.26 V and short-circuit current (I_{SC}) of 5.70 $\mu\text{A cm}^{-2}$ under 95 % relative humidity (RH), which decay quickly (black line in Fig. 2e). This is because the pristine graphite electrode lacks ion storage sites, thus having low ion-electron conversion capability. Upon storing a few ions, a voltage surge will occur at the functional layer/electrode interfaces, subsequently impeding further ion migration. When the capacitive MnO_2 and MoS_2 are decorated on the graphite electrode (MEH_M), the V_{OC} and I_{SC} jump to 0.68 V and 6.27 mA cm^{-2} under 95%RH, which attenuate significantly more slowly (red line in Fig. 2e). The larger V_{OC} and I_{SC} are attributed to the increased ion storage on the interface. The slower decay rate is ascribed to the restraint on the formation of the built-in electric field caused by the improved ion-electron conversion. Furthermore, when the redox couples are introduced at the PSS layer/electrode interface, the electrical output is further promoted to 0.72 V and 9.24 mA cm^{-2} under 95%RH, and the V_{OC} exhibits no decline (blue line in Fig. 2e). The electrons transferred through faradic process will take part in the interfacial charge balance, stabilizing the electrode potential while enabling more ions to be stored on the electrode. As a result, both the V_{OC} and maximum I_{SC} are even approaching the levels of perovskite solar cells (10–20 mA cm^{-2} , ~ 1.1 V)^{22–25}.

However, the output charge of *i*-eMEH calculated from the integral area of the I_{SC} -time curve soon reaches a platform of 0.87 C (Supplementary Fig. 8), close to the *i*-eMEH charge storage utmost (0.92 C, Fig. 2f and Supplementary Fig. 9, Method). This indicates that the electric generation performance is still restricted. Therefore, a quasi-continuous working mode is designed to realize more ion storage in the single moisture-enabled electric generation process. After being exposed to moisture, *i*-eMEH can be self-charged in an open-circuit state, and discharged by connecting to an external circuit. Whereafter, the voltage of *i*-eMEH will be fully recovered when switching back to the open-circuit state again, and goes through a cyclic discharge process. The V_{OC} of 0.79 V, I_{SC} of 7.44 mA cm^{-2} can be achieved in this quasi-continuous output manner (Fig. 2g, h). The accumulated output charge reaches 1.43 C within 120,000 s, significantly higher than the charge storage utmost and that under continuous output mode (Fig. 2f and Supplementary Fig. 8). Similarly, the output energy maintains steady growth under quasi-continuous output, differing from the plateau under continuous output (Fig. 2i), which manifests that the quasi-continuous output largely improves the discharge ability. Although the electric generation will degenerate with the extension of output time induced by the even distribution of anions and cations in the membrane motivated by the thermal movement of ions (Supplementary Fig. 10), the *i*-eMEH can be reactivated by removing the moisture field and totally drying the *rc*-PSS membrane after discharging. The reactivated *i*-eMEH recovers the voltage and current after re-exposure to the moisture field, and only exhibits slight decrease after multiple cycles (Supplementary Fig. 11).

The contribution of increased capacitance and faradic process to electrical output performance is further estimated by comparing the

I_{SC} and cumulative output charge of MEH_g , MEH_M , and *i*-eMEH (Supplementary Fig. 12 and Supplementary Note 3). The contribution ratio of increased capacitance and faradic process to I_{SC} is 36.9% and 60%, and to cumulative charge within 12 h ($\text{Charge}_{12\text{ h}}$) is 49.1% and 50.9% (Fig. 2j). It is noteworthy that the cumulative charge increases from 0.42 C to 0.86 C within 12 h with the addition of redox couples. The increment is far greater than that of unidirectional reaction of redox couples (0.02 C). This indicates that the redox couples are not consumable, but carry out bidirectional reactions to assist the ion-electron conversion in the interface like “electron sponge” (Supplementary Note 3 and 1c). Furthermore, *i*-eMEH delivers a maximum power density of 6.69 W m^{-2} at 47 Ω (Fig. 2k), exceeding previous moisture-enabled electric generators and hydrovoltaic generators by an order of magnitude (Fig. 2l and Supplementary Table 1). Notably, the maximum power density is superior to the thermo-electric effect of polymer^{40,41}, being on par with thermogalvanic cells^{26,27,42}, and even the thermo-electric effect of SnSe system (Supplementary Table 2 and Supplementary Note 4)^{28,43,44}. This manifests that the same level of electrical output can be attained from moisture energy as from thermal energy through ion-electron conversion enhanced interface design.

To further clarify the effect of redox couples on ion-electron conversion, the oxidant/reductant ratio and quantity of redox couples within *i*-eMEH are systematically studied (Supplementary Figs. 13 and 14). The electrical output ranks the best when the oxidant/reductant ratio is close to 1: 1 (Supplementary Fig. 13). Since oxidant possesses the ability to gain electrons, while reductant shows the ability to lose electrons, the coexistence of oxidant and reductant in redox couples has the strongest ability to transfer electrons in two directions. The quantity of the redox couples at the *rc*-PSS/electrode interface determines the charge transfer intensity. As the redox couple quantity increases, I_{SC} first increases from 2.53 to 7.44 mA induced by the enhanced ion-electron interaction, but then slightly declines, caused by the decreased reversibility of the redox reaction (Supplementary Fig. 14)⁴². Moreover, whether the redox couples are symmetrical or asymmetric, and how the asymmetric redox couples are arranged, the electric generation is higher than that without redox couples (Supplementary Fig. 15). Further experiments about the influence of redox couple distribution, *rc*-PSS layer and capacitive interface layer thickness on electric generation performance are conducted for performance optimization (Supplementary Figs. 16–20).

Mechanism verification of electricity generation

The electron transfer process is directly reflected by the variation of electrode potentials. The in situ record exhibits that the electrode potential of MnO_2 increases to 1.39 V and that of MoS_2 decreases to 0.53 V after being exposed to moisture, suggesting the directional migration of cations (H^+) from MoS_2 to MnO_2 electrode in *rc*-PSS (Fig. 3a and Supplementary Fig. 21). The redox potentials of I_3^-/I^- and $[\text{Fe}(\text{CN})_6]^{3-/4-}$ in *rc*-PSS are measured to be 0.67 V and 0.63 V, respectively (Fig. 3a and Supplementary Fig. 22). The detected potentials signify that I_3^-/I^- undergoes reduction reaction, transferring electrons to the MnO_2 electrode, and $[\text{Fe}(\text{CN})_6]^{3-/4-}$ undergoes oxidation reaction, receiving electrons from the MoS_2 electrode (Fig. 3a). The potential of MnO_2 electrode and I_3^-/I^- redox couple ($\text{MnO}_2\text{-I}$) is 1.38 V, and that of MoS_2 electrode and $[\text{Fe}(\text{CN})_6]^{3-/4-}$ redox couple ($\text{MoS}_2\text{-Fe}$) is 0.62 V, validating the above discussion (Fig. 3b and Supplementary Fig. 23). At the short-circuit state, electrons will transfer from $\text{MnO}_2\text{-I}$ side to $\text{MoS}_2\text{-Fe}$ side. The decline in the potential of $\text{MnO}_2\text{-I}$ side and the increase in the potential of $\text{MoS}_2\text{-Fe}$ side at short-circuit state confirm the reversed electron transfer direction (Fig. 3b). Therefore, the redox couples act as “electron sponges” to provide and receive electrons to assist the storage of the ions induced by the moisture field (Fig. 1c and Supplementary Fig. 1b).

The potentials recover when switching back to the open-circuit state and exhibit good cyclic stability (Fig. 3b), which signifies that

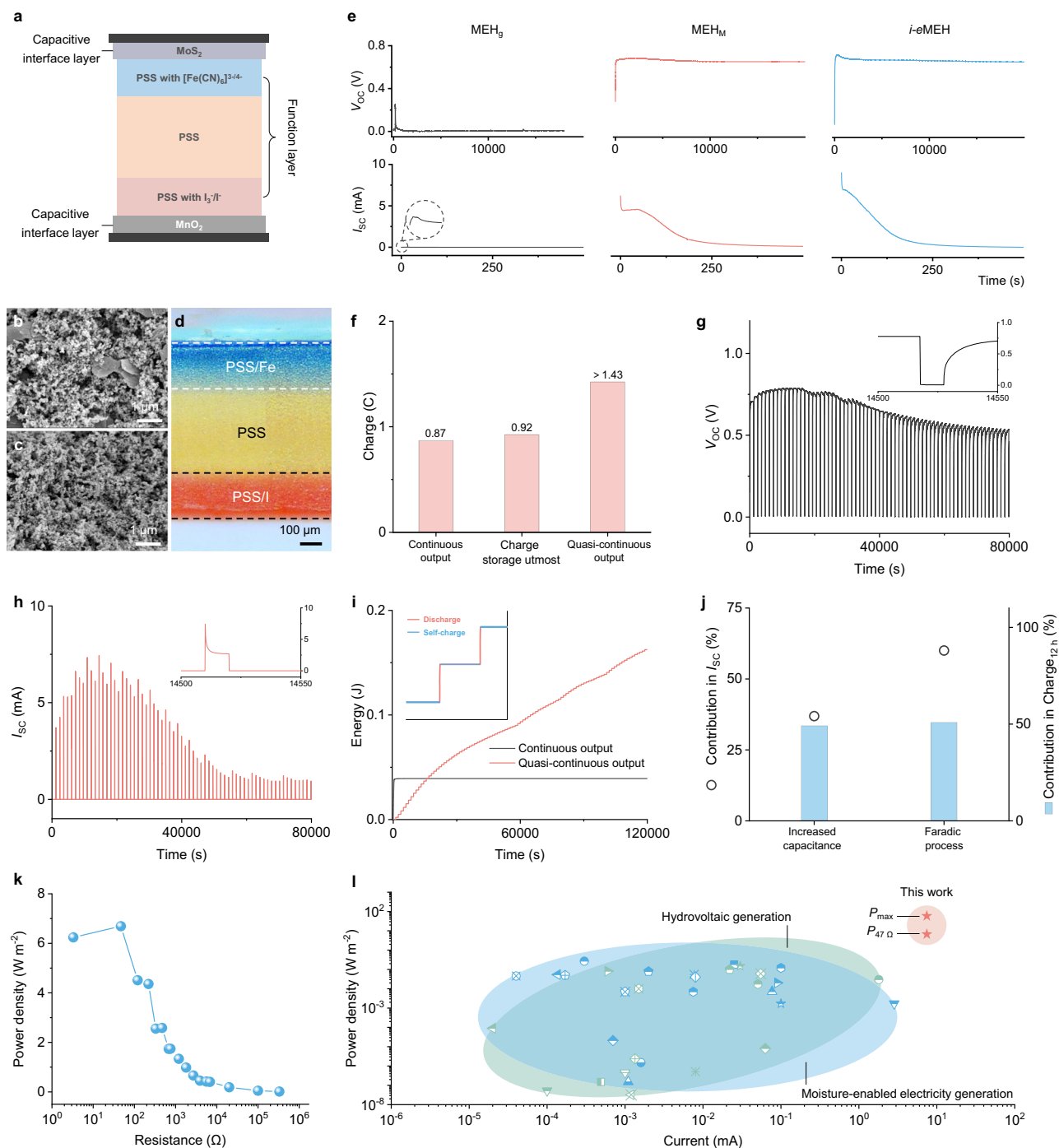
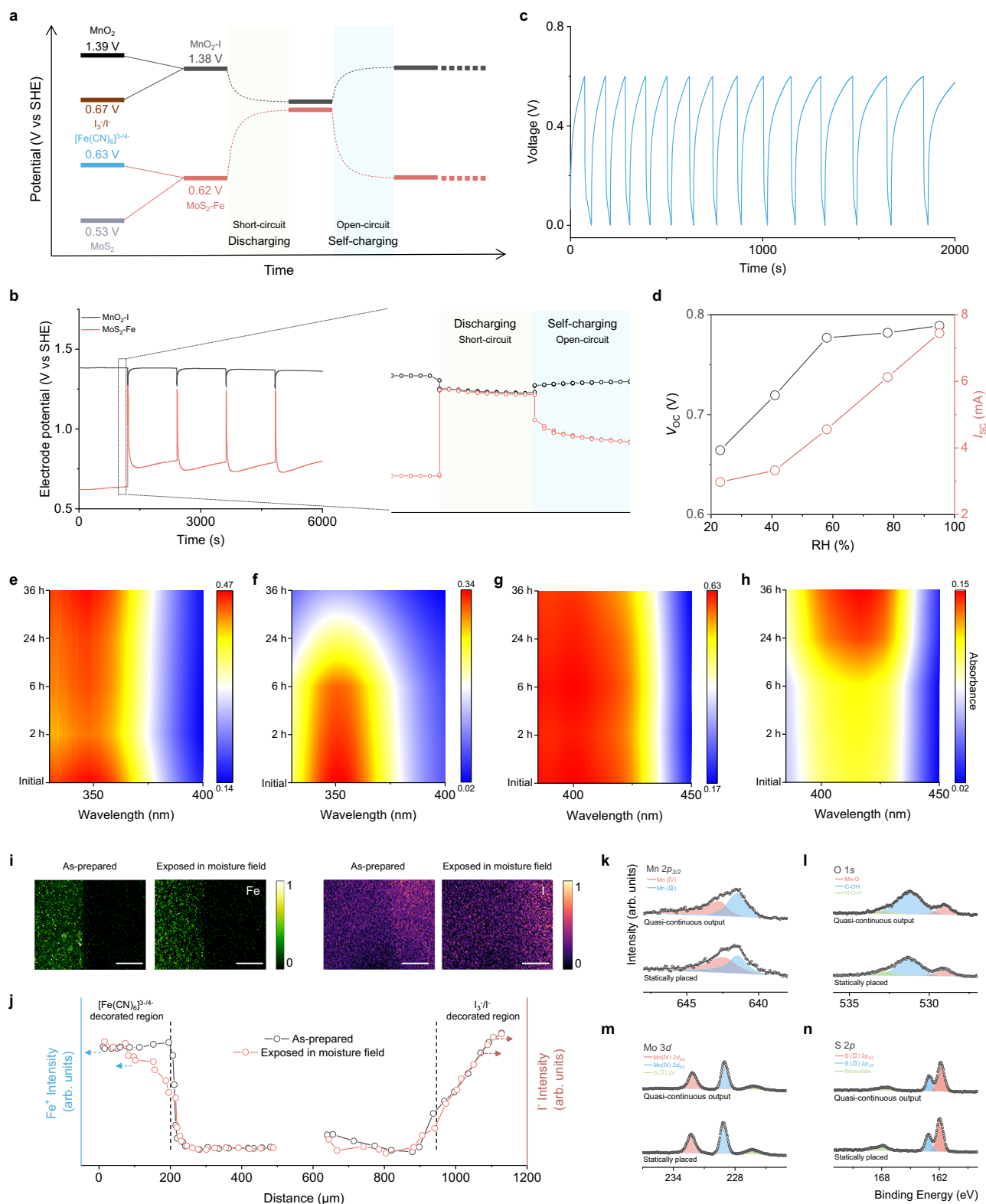


Fig. 2 | Structure and electrical generation performance of *i*-eMEH. **a** Schematic diagram of *i*-eMEH. PSS is the polystyrene sulfonic acid doped with sulfuric acid. **b, c** SEM images of MoS₂ and MnO₂ electrodes, respectively. **d** Optical image of the cross-section of *rc*-PSS layer. The PSS/I layer is colored by the addition of methyl orange. All the colors are actual colors. **e** V_{OC}-time curves (top) and I_{SC}-time curves (bottom) of MEH_g (black line), MEH_M (red line), and *i*-eMEH (blue line). MEH_g is the moisture energy harvester based on PSS sandwiched between graphite electrode, and MEH_M is the moisture energy harvester based on PSS sandwiched between MoS₂ electrode and MnO₂ electrode. **f** The output charge of *i*-eMEH under continuous output and quasi-continuous output for 200,000 s when loaded 47 Ω resistor, as well as the charge storage utmost of *i*-eMEH. The V_{OC}-time (g) and I_{SC}-time curves (h) of *i*-eMEH. Insets show the enlarged details of the V_{OC}-time and I_{SC}-time curves.

time curves. The inset axes share the units of the main figures. **i** The energy-time curves of *i*-eMEH under continuous output and quasi-continuous output with 47 Ω load resistor. Inset shows the enlarged energy-time curve under quasi-continuous output. The inset axes share the units of the main figure. **j** The contribution of increased capacitance and faradic process on I_{SC} and accumulated charge at 80,000 s. **k** The relation between power density and load resistance. **l** The performance comparison chart of *i*-eMEH in relation to other moisture-enabled electric generators and hydrovoltaic devices. P_{max} is calculated from V_{OC} × I_{SC}, and the P_{47 Ω} is the power density with 47 Ω loaded resistance. The points correspond to Supplementary Table 1. The electrical output was tested under 95%RH. All the experiment results were repeated independently at least three times.



moisture-induced directional ion migration is capable of driving “electron sponges” to operate periodically. The self-recovery ability of *i*-eMEH is further verified by the galvanostatic discharge tests. *i*-eMEH can self-charge spontaneously to 0.6 V after being fully discharging to 0 V (Fig. 3c). Notably, the relative humidity (RH) increase is more effective in recovering the electrode potentials, and all the V_{OC} , I_{SC} , and energy conversion efficiency are improved, implying the dominant role of the driving force from

moisture (Fig. 3d, Supplementary Figs. 24 and 25, and Supplementary Note 5).

The reactions of redox couples are also tracked by UV-vis absorption spectroscopy (Method). Due to the strong ultraviolet absorption of PSS, only I₃⁻ (357 nm) and [Fe(CN)₆]³⁻ (420 nm) can be directly detected (Supplementary Figs. 26 and 27, Supplementary Note 6). As depicted in Fig. 3e, the absorbance of I₃⁻ shows no significant change. However, the unidirectional electron transfer will lead

Fig. 3 | Mechanism verification of electricity generation. **a** The potential evolution diagram of MnO_2 (black line) and MoS_2 electrode (purple line) on PSS layer in reference to standard hydrogen electrode (SHE) before and after being exposed to moisture. The evolution diagram of potential of MnO_2 and I_3^-/I^- redox couple (MnO_2/I , gray line), and equilibrium potential of MoS_2 and $[\text{Fe}(\text{CN})_6]^{3-/4-}$ redox couple (MoS_2/Fe , red line) during the quasi-continuous output. **b** The potential cyclic variation of MnO_2/I and MoS_2/Fe under quasi-continuous operation. **c** Voltage recovery curve of *i*-eMEH under $100 \mu\text{A cm}^{-2}$ discharge current and $0 \mu\text{A cm}^{-2}$ charged current. The *i*-eMEH was fully discharged at $100 \mu\text{A cm}^{-2}$ current density before test. **d** The V_{OC} and I_{SC} of *i*-eMEH under different RH. **e** The evolution of UV-vis absorption spectra of I_3^- during quasi-continuous output. **f** The evolution of UV-vis absorption spectra of I_3^- during incessant output. **g** The evolution of UV-

vis absorption spectra of $[\text{Fe}(\text{CN})_6]^{3-}$ during quasi-continuous output. **h** The evolution of UV-vis absorption spectra of $[\text{Fe}(\text{CN})_6]^{3-}$ during incessant output. **i** The TOF-SIMS images of Fe^+ at the interface between PSS/Fe and PSS layer, and the TOF-SIMS images of I^- ion in the interface between PSS and PSS/I layer in the as-prepared *rc*-PSS layer and the *rc*-PSS layer after being exposed in moisture field for 2 h. Scale bar: $100 \mu\text{m}$. **j** Line scan profiles of Fe^+ ion in the interface between PSS/Fe and PSS layer, and the line scan profile of I^- ion in the interface between PSS and PSS/I layer in the as-prepared *rc*-PSS layer and the *rc*-PSS layer after being exposed in moisture field for 2 h. The scanning area is $500 \times 500 \mu\text{m}^2$. XPS fine spectroscopy for Mn $2p_{3/2}$ (**k**) and O $1s$ (**l**) of MnO_2 electrode placed statically and after quasi-continuous output. XPS fine spectroscopy for Mo $3d$ (**m**) and S $2p$ (**n**) of MoS_2 electrode placed statically and after quasi-continuous output.

to the continuous decrease in I_3^- and increase in I^- (Fig. 3f, Supplementary Fig. 28a and Supplementary Note 7). Therefore, it can be inferred that the stable spectra of I_3^- in Fig. 3e are attributed to the bidirectional electron transfer between the I_3^-/I^- and MnO_2 electrode. The same conclusion applies to $[\text{Fe}(\text{CN})_6]^{3-/4-}$ at the MoS_2 electrode interface (Fig. 3g, h and Supplementary Fig. 28b).

To further demonstrate the non-interaction of redox couples within the *rc*-PSS, the distributions of the redox couples are detected by Time of Flight Secondary Ion Mass Spectrometry (TOF-SIMS). The Fe element shows no cross-layer migration after exposure to the moisture field (Fig. 3i, j). Similarly, the distribution of I element at the interface of PSS and PSS/I layers exhibits no significant variation (Fig. 3i, j). The cation selectivity of the PSS layer in the middle plays a pivotal role in blocking the migration of anions. Furthermore, the optical cross-section images of the as-prepared *rc*-PSS layer and those exposed to the moisture field exhibit no change (Supplementary Fig. 29). These results coherently demonstrate that the redox couples only transfer electrons at the *rc*-PSS/electrode interface.

The increased ion storage capacity in the interface is confirmed by the improved capacitance of MnO_2 and MoS_2 electrodes (Supplementary Fig. 30). Furthermore, X-ray photoelectron spectroscopy (XPS) confirms the stability of electrode materials (Fig. 3k–n). The ratio of Mn(III) (−641.4 eV) and Mn(IV) (−642.5 eV) of MnO_2 electrode after quasi-continuous output does not change compared to that placed in quiescence, indicating no valence change in MnO_2 (Fig. 3k and Supplementary Table 3). The lattice oxygen (−529 eV) and adsorbed oxygen (−531 eV and −533 eV) also show no obvious variation after quasi-continuous output (Fig. 3l, Supplementary Fig. 31b, c, and Supplementary Table 4). The peaks of Mo(IV) $3d_{5/2}$ (−229 eV), $3d_{3/2}$ (−232 eV) in Fig. 3l, and the peak of S(II) $2p_{3/2}$ (−161.9 eV), $2p_{1/2}$ (−163 eV) in Fig. 3m attributed to the 2H- MoS_2 exhibit no shift after quasi-continuous output, demonstrating the stability of MoS_2 electrode (Fig. 3m, n and Supplementary Tables 5 and 6).

Application potential in off-grid energy and miniaturized flexible electronics

The electrical generation performance can be further enhanced by enlarging the unit and integration. The voltage remains stable with the increase in area, and the current linearly enhances because of the increase in directionally migrating ions (Fig. 4a and Supplementary Fig. 32). The integration is capable of further elevating the *i*-eMEH performance to a whole new level. The MnO_2 and MoS_2 electrodes can be fabricated through scalable blade coating (Supplementary Fig. 33a, b), and the *rc*-PSS layer can be obtained through a casting method and subsequent layer-by-layer stacking (Supplementary Fig. 33c–e). Both the electrodes and layer can be machined by laser into the required shape, and assembled into *i*-eMEH, enabling rapid integration by repeated stacking to meet the practical power supply requirements (Supplementary Fig. 33). Connecting thirty units in series readily generates a high voltage of 22 V, and the series voltage increases linearly with the number of units (Fig. 4b and Supplementary Fig. 34). Forty units connected in parallel deliver a current of 0.39 A, with

parallel current increasing linearly with the number of parallel units, demonstrating excellent integration performance (Fig. 4c and Supplementary Fig. 35).

Benefiting from the high performance of *i*-eMEHs, the supplied electric power can be stored in commercial capacitors and batteries on demand. For example, the high-capacitance capacitor of 4 F can be charged by assembled 3×10 array to −1 V (Fig. 4d), an achievement unachievable with previous integrated moisture-electricity generators that could only charge microfarad and millifarad capacitors^{29,45}. An integrated 7×6 array can easily charge the commercial lithium battery LIR1025 (Supplementary Fig. 36), which can then actuate a commercial electric fan (JISULIFE LA19, 3 W) working in four modes (Fig. 4e and Supplementary Video 1). Furthermore, *i*-eMEH unit exhibits good mechanical strength, which can maintain stable electrical generation after bending 45° and under different pressure (Supplementary Fig. 37 and 38). The performance of the flexible *i*-eMEH unit is already better than the flexible silicon solar cells (0.76 V , 0.33 mA cm^{-2})⁴⁶, and the flexible thermoelectric devices (70 mW m^{-2} , $\Delta T = 44 \text{ K}$)⁴⁷. Combined with the superior power density, *i*-eMEH demonstrates the potential in the field of miniaturized flexible electronic chips. Four *i*-eMEH units assembled in series (0.25 cm^2) on flexible printed circuit board can charge a capacitor of $220 \mu\text{F}$ to 2 V in the ambient environment and then light the LED (Fig. 4f, g and Supplementary Video 2). Previously, it often took dozens of $1 \times 1 \text{ cm}^2$ devices to light the LED^{47,48}. *i*-eMEH is also applicable in a wide range of -18°C to 60°C (Supplementary Fig. 39). These demonstrations illustrate the significant role of *i*-eMEH in powering miniaturized flexible electronics and mark a pivotal stride forward in the practical applications of moisture energy harvesters.

Discussion

In summary, we develop an ion-electron conversion-enhanced strategy that achieves an order-of-magnitude improvement in moisture electricity generation. The formation of ion storage sites and introduction of redox couples at the interfaces not only enhance electrode capacitance but also facilitate a synergistic faradic process. As a result, the *i*-eMEH realizes a record-high current of 9.2 mA cm^{-2} and power density of $\sim 6.7 \text{ W m}^{-2}$, 60 times higher than previously reported moisture-enabled generators and comparable to solar cells and thermoelectric devices. Furthermore, *i*-eMEH demonstrates preliminarily potential for miniaturized flexible electronic chips. The performance of flexible *i*-eMEH unit is superior to that of flexible silicon solar cells and flexible thermoelectric devices. This work takes an important step forward in the practical implementation of moisture energy harvester and provides an opportunity for the development of miniaturized power supply systems.

Methods

Preparation of materials

Preparation of electrode. Polyvinylidene fluoride (PVDF) binder was prepared by dissolving 10 g PVDF (Bidepharm) in 500 ml 1-Methyl-2-pyrrolidinone (NMP, Meryer, 99.5%, Energy Chemical, 99.5%) via vigorous stirring using magnetic stirrers at room temperature for 24 h. For the preparation of the working electrodes, 70 wt% electroactive

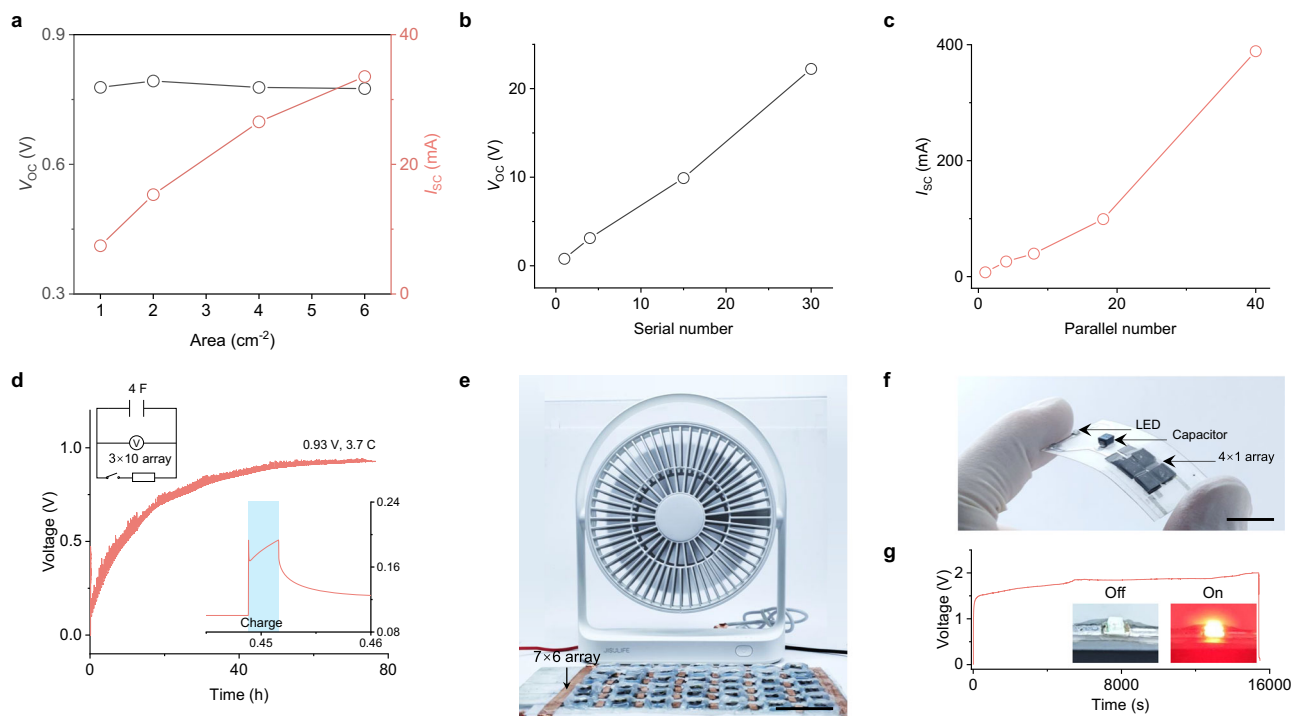


Fig. 4 | Application of *i*-eMEH. **a** The V_{OC} and I_{SC} of *i*-eMEH with different area. **b** The V_{OC} of *i*-eMEH array with different serial number. Each *i*-eMEH unit is $1 \times 1 \text{ cm}$. **c** The I_{SC} of *i*-eMEH array with different parallel number. Each *i*-eMEH unit is $1 \times 1 \text{ cm}$. **d** Voltage-time curve of commercial capacitors (4 F) charged by 4×2 *i*-eMEH arrays (4 in series and 2 in parallel) under quasi-continuous output (10 s/20 min). Inset exhibits the circuit connection diagram and the enlarged voltage-time curve in single cycle of quasi-continuous output. The inset axes share the units of the main

figure. **e** Optical image of the commercial electric fan (JISULIFE LA19) actuated by a lithium battery LIR1025 charged by 7×6 *i*-eMEH arrays. Scale bar: 3 cm. **f** Optical image of the flexible circuit composed of a resistance, capacitor (220 μF), four *i*-eMEH units (0.25 cm^2) connected in series, and an LED light bead. Scale bar: 1 cm. **g** The voltage-time curve of the capacitor (220 μF) on flexible circuit charged by 4×1 *i*-eMEH array (1 cm^2). Inset depicts the LED light in the off and on states, respectively.

material, 20 wt% Super P (Timical), and 10 wt% PVDF binder were first grounded in a mortar to form a homogeneous slurry. Manganese dioxide (MnO_2 , Meryer, 99%) and Molybdenum sulfide (MoS_2 , Meryer, 99.5%, $<2 \mu\text{m}$) were used for MnO_2 and MoS_2 electrodes, respectively. The slurry was cast onto graphite foil (Fuel Cells Etc, 25 μm in thickness) as the current collector, and dried in an oven at 60 $^\circ\text{C}$. The typical thickness of MnO_2 electrode and MoS_2 electrode were 12 μm . The MoS_2 electrode (1 $\text{cm} \times 1 \text{ cm}$) was laser-drilled to form four holes with diameter of 4 mm, so the effective area of a 1 cm^2 MoS_2 electrode is 0.49 cm^2 . All areas used in calculations are determined by the area of the MnO_2 electrode.

Preparation of functional layer. An aqueous Polystyrene sulfonic acid dispersion (PSS, 30 wt% in water, Mw ~75,000, Energy Chemical) was uniformly mixed with 0.05 M H_2SO_4 (95.0–98.0%, Peking Reagent) with the same volume (abbreviated as PSS layer solution). The PSS layer solution was uniformly mixed with an aqueous solution containing 5 mM $\text{K}_3[\text{Fe}(\text{CN})_6]$ (Meryer, 99%) and 5 mM $\text{K}_4[\text{Fe}(\text{CN})_6]$ (Meryer, 99%) at the volume ratio of 2:1 (abbreviated as PSS/Fe layer solution). Similarly, the PSS layer solution was uniformly mixed with an aqueous solution containing 1.25 mM I_2 (Energy Chemical, 99.8%) and 5 mM KI (Bidepharm, 99.19%, Alfa Aesar, 99.9%) at a volume ratio of 2:1 (abbreviated as PSS/I layer solution). The PSS, PSS/Fe, and PSS/I layer solutions were cast into petri dishes and dried in a vacuum oven at 45 $^\circ\text{C}$ under 60% RH to prepare PSS, PSS/Fe, and PSS/I layers. Then, the PSS/Fe layer, PSS layer, and PSS/I layer were stacked layer by layer to form the *rc*-PSS layer.

Preparation of ion-electron conversion enhanced moisture energy harvester (*i*-eMEH). The *rc*-PSS layer was sandwiched between MoS_2 electrode and MnO_2 electrode, and the assembly was sealed with hot-melt resin except for the pores in MoS_2 electrode.

Characterization

Scanning electron microscope (SEM) images were acquired using Hitachi cold-field emission scanning electron microscopes. Energy dispersive X-ray spectra (EDS) were performed with an INCA Energy EDS System (Oxford Instruments, UK). Time of Flight Secondary Ion Mass Spectrometry (TOF-SIMS) was conducted using a TOF.SIMS 5-100 (ION-TOF GmbH, Germany). X-ray photoelectron spectroscopy (XPS) was performed on an ESCALAB Xi⁺ photoelectron spectrometer (Thermo Fisher) with an Al K α source. Element analysis was carried out using an inductively coupled plasma optical emission spectrometer (Thermo, IRIS Intrepid II, United States). UV-vis absorption spectra were recorded using an ultraviolet spectrophotometer (Agilent, Cary 5000, USA). Inductively coupled plasma-optical emission spectrometry (ICP-OES) measurements were performed on an IRIS Intrepid II (Thermo, USA). The solid surface zeta potential was measured using an electrokinetic analyzer for solid surface analysis (SurPASS 3, Anton Paar, Austria). Mechanical strength was tested using an electronic universal testing machine (CMT6103, Metus, America).

Device characterization

Electrical output performance measurement. The electrical output measurements were performed with Keithley 2400 and Keithley 2612b (Keithley Instruments). The circuit parameter of current during the voltage output test was 0 nA, and the circuit parameter of voltage during the current output test was 0 V. The cumulative output energy is calculated through $\int I^2 R dt$, where R and I are the loaded resistance and the current on the loaded resistance, respectively. The cumulative no-load energy is calculated through $\int I_{SC}^2 dt$. All the experiment results were independently repeated at least three times.

Electrochemical measurement. The electrochemical performance of electrodes was characterized using a three-electrode configuration, where the prepared electrode, a platinum sheet, and an Ag/AgCl electrode (for neutral solution) or Hg/Hg₂SO₄ electrode (for acid solution) served as the working electrode, counter-electrode, and reference electrode, respectively. Electrochemical measurements were conducted on an electrochemical workstation (CHI 660d and CHI 660e). Galvanostatic charge/discharge (GCD) tests were performed at a discharge current of 100 $\mu\text{A cm}^{-2}$ and a charge current of 0 $\mu\text{A cm}^{-2}$ to evaluate the self-recovery performance of *i*-eMEH. Electrochemical impedance spectroscopy (EIS) was carried out in the frequency range 0.1–100 kHz, with a 5 mV alternating current (a.c.) amplitude. The area capacitance (C_A) was calculated using the following equation:

$$C_A(f) = -\frac{Z''(f)}{2\pi Af|Z(f)|^2} \quad (1)$$

where $Z''(f)$ is the real part and imaginary part of impedance $Z(f)$ at a specified frequency f . A is the area of the electrode. All the experiment results were independently repeated at least three times.

Intrinsic capacity of *i*-eMEH. To characterize the intrinsic capacitance of *i*-eMEH, an H-type electrolytic cell was constructed. On one side, the MnO₂ electrode (1 cm²) was immersed in 50 mL deionized water containing a 1 cm² PSS/I layer (370 μm) and 1 cm² PSS layer (370 μm). On the other side, the MoS₂ electrode (1 cm²) was immersed in 50 mL deionized water containing a 1 cm² PSS/Fe layer (370 μm) and a 1 cm² PSS layer (370 μm). The device was first galvanostatic charged to 0.7 V at a current density of 1 mA cm⁻², then connected to a 47 Ω resistor for discharge until the current dropped below 1 $\mu\text{A cm}^{-2}$. The intrinsic capacitance was calculated from the integrated area of the discharge-time curve.

TOF-SIMS measurement. As for Fe scanning, TOF-SIMS dual-beam depth profiling was performed on *rc*-PSS using a bunched Bi⁺ gun at high-energy (30 keV) as primary beam from incident angle of 45° with the scanning area of 500 $\mu\text{m} \times 500 \mu\text{m}$. The secondary ion polarity is cation with mass ranging from 0 to 900 amu. The O₂⁺ with low-energy (1 keV) and the sputtering speed of 0.16 nm s⁻¹ (for SiO₂) from incident angle of 45° as sputtering guns.

As for I scanning, TOF-SIMS dual-beam depth profiling was performed on *rc*-PSS using a bunched Bi⁺ gun at high-energy (30 keV) as primary beam from incident angle of 45° with the scanning area of 500 $\mu\text{m} \times 500 \mu\text{m}$. The secondary ion polarity is anion with mass ranging from 0 to 900 amu. The Cs⁺ with low-energy (2 keV) and the sputtering speed of 0.057 nm s⁻¹ (for SiO₂) from incident angle of 45° as sputtering guns.

UV-vis absorption spectra measurement. The behavior of redox couples was detected by UV-vis absorption spectroscopy in an H-type electrolytic cell containing PSS/I and PSS/Fe solutions, with MnO₂ and MoS₂ electrodes immersed in the two sides. The initial volume of both PSS/Fe and PSS/I layer solutions was 75 mL, and 3 mL was sampling for each test. Each sampled solution was mixed with an equal volume of deionized water to prepare the detection solution, ensuring compliance with the quantitative requirements of the Lambert-Beer law:

$$A = \lg(I_0/I_t) = \lg(1/T) = Klc \quad (2)$$

Where I_0 , I_t and T are incident monochromatic light intensity, transmittance light intensity and transmission ratio, respectively. l , c , and K are the optical path length, the concentration of the absorbent substance, and the molar absorption coefficient of the absorbent substance, respectively.

The reason why *i*-eMEH can be approximately replaced by H-type electrolytic cell is that the hydroxyl group on MnO₂ electrode will undergo protonation reaction and be positively charged during solid-liquid contact, while hydroxyl group on MoS₂ will undergo deprotonation reaction and be negatively charged. Therefore, a potential difference will be established. The surface zeta potentials of MnO₂ electrode and MoS₂ electrode are 31 mV and -9 mV, respectively, further proving the asymmetrically charge state. The potentials of MnO₂ electrode and MoS₂ electrode are 1.9 V and 0.58 V, respectively, in PSS layer solution. Furthermore, it is known that the electron work function has similar values for MnO₂ and MoS₂ (4.6 eV and 4.59 eV)^{49,50}, so that the voltage drop between MnO₂ and MoS₂ junction can be considered negligible. The electrode potential difference is capable of driving the redox couples to undergo bidirectional electron transfer, the mechanism of which is the same like that of *i*-eMEH. The difference is that the directional ion migration induced by the moisture field can further increase the electrode potential difference, thus increasing the driving force of bidirectional redox reaction.

Reporting summary

Further information on research design is available in the Nature Portfolio Reporting Summary linked to this article.

Data availability

Source data are provided with this paper. Additional data related to this work are available from the corresponding authors upon request. Source data are provided with this paper.

References

- Shen, D. et al. Moisture-enabled electricity generation: from physics and materials to self-powered applications. *Adv. Mater.* **32**, 2003722 (2020).
- Macha, M., Marion, S., Nandigana, V. V. R. & Radenovic, A. 2D materials as an emerging platform for nanopore-based power generation. *Nat. Rev. Mater.* **4**, 588–605 (2019).
- Zhang, Z., Wen, L. & Jiang, L. Nanofluidics for osmotic energy conversion. *Nat. Rev. Mater.* **6**, 622–639 (2021).
- Hochbaum, A. I. & Yang, P. Semiconductor nanowires for energy conversion. *Chem. Rev.* **110**, 527–546 (2010).
- Masseti, M. et al. Unconventional thermoelectric materials for energy harvesting and sensing applications. *Chem. Rev.* **121**, 12465–12547 (2021).
- Pan, C., Zhai, J. & Wang, Z. L. Piezotronics and piezo-phototronics of third generation semiconductor nanowires. *Chem. Rev.* **119**, 9303–9359 (2019).
- Wu, W. & Wang, Z. L. Piezotronics and piezo-phototronics for adaptive electronics and optoelectronics. *Nat. Rev. Mater.* **1**, 16031 (2016).
- Zhang, Z. et al. Emerging hydrovoltaic technology. *Nat. Nanotechnol.* **13**, 1109–1119 (2018).
- Xu, J. et al. Sustainable moisture energy. *Nat. Rev. Mater.* **9**, 22–737 (2024).
- Xu, T., Ding, X., Cheng, H., Han, G. & Qu, L. Moisture-enabled electricity from hygroscopic materials: a new type of clean energy. *Adv. Mater.* **35**, 2209661 (2023).
- Huang, Y., Cheng, H. & Qu, L. Emerging materials for water-enabled electricity generation. *ACS Mater. Lett.* **3**, 193–209 (2021).
- Bai, J., Huang, Y., Cheng, H. & Qu, L. Moist-electric generation. *Nanoscale* **11**, 23083–23091 (2019).
- Zhao, F., Cheng, H., Zhang, Z., Jiang, L. & Qu, L. Direct power generation from a graphene oxide film under moisture. *Adv. Mater.* **27**, 4351–4357 (2015).
- Liu, X. et al. Power generation from ambient humidity using protein nanowires. *Nature* **578**, 550–554 (2020).

15. Xu, T. et al. An efficient polymer moist-electric generator. *Energy Environ. Sci.* **12**, 972–978 (2019).
16. Huang, Y. et al. Interface-mediated hygroelectric generator with an output voltage approaching 1.5 volts. *Nat. Commun.* **9**, 4166 (2018).
17. Wang, H. et al. Moisture adsorption-desorption full cycle power generation. *Nat. Commun.* **13**, 2524 (2022).
18. Yang, M. et al. Fabrication of moisture-responsive crystalline smart materials for water harvesting and electricity transduction. *J. Am. Chem. Soc.* **143**, 7732–7739 (2021).
19. Yang, L., Zhang, L., Cui, J. & Sun, D. Tailoring MXene-based films as moisture-responsive actuators for continuous energy conversion. *J. Mater. Chem. A* **10**, 15785–15793 (2022).
20. Wu, K. et al. Neuron-inspired self-powered hydrogels with excellent adhesion, recyclability and dual-mode output for multifunctional ionic skin. *Adv. Funct. Mater.* **33**, 2300239 (2023).
21. He, D. et al. Electricity generation from phase-engineered flexible MoS₂ nanosheets under moisture. *Nano Energy* **81**, 105630 (2021).
22. Zhang, Z. et al. Suppression of phase segregation in wide-bandgap perovskites with thiocyanate ions for perovskite/organic tandems with 25.06% efficiency. *Nat. Energy* **9**, 592–601 (2024).
23. Azmi, R. et al. Double-side 2D/3D heterojunctions for inverted perovskite solar cells. *Nature* **628**, 93–98 (2024).
24. Liu, S. et al. Triple-junction solar cells with cyanate in ultrawide-bandgap perovskites. *Nature* **628**, 306–312 (2024).
25. Nayak, P. K., Mahesh, S., Snaith, H. J. & Cahen, D. Photovoltaic solar cell technologies: analysing the state of the art. *Nat. Rev. Mater.* **4**, 269–285 (2019).
26. Yu, B. et al. Thermosensitive crystallization-boosted liquid thermocells for low-grade heat harvesting. *Science* **370**, 342–346 (2020).
27. Wang, Y. et al. In situ photocatalytically enhanced thermogalvanic cells for electricity and hydrogen production. *Science* **381**, 291–296 (2023).
28. Su, L. et al. High thermoelectric performance realized through manipulating layered phonon-electron decoupling. *Science* **375**, 1385–1389 (2022).
29. Li, P. et al. Multistage coupling water-enabled electric generator with customizable energy output. *Nat. Commun.* **14**, 5702 (2023).
30. Liu, X., Gao, H., Sun, L. & Yao, J. Generic Air-Gen Effect in Nanoporous Materials for Sustainable Energy Harvesting from Air Humidity. *Adv. Mater.* **35**, 2300748 (2023).
31. Yao, B. et al. Ultrastrong, highly conductive and capacitive hydrogel electrode for electron-ion transduction. *Matter* **5**, 4407–4424 (2022).
32. Fang, Y. et al. Micelle-enabled self-assembly of porous and monolithic carbon membranes for bioelectronic interfaces. *Nat. Nanotechnol.* **16**, 206–213 (2021).
33. Li, Z. et al. Tuning the interlayer spacing of graphene laminate films for efficient pore utilization towards compact capacitive energy storage. *Nat. Energy* **5**, 160–168 (2020).
34. Yang, X., Cheng, C., Wang, Y., Qiu, L. & Li, D. Liquid-mediated dense integration of graphene materials for compact capacitive energy storage. *Science* **341**, 534–537 (2013).
35. Zhang, Y. et al. Sustainable power generation for at least one month from ambient humidity using unique nanofluidic diode. *Nat. Commun.* **13**, 3484 (2022).
36. Xie, P., Rong, M. Z. & Zhang, M. Q. Moisture battery formed by direct contact of magnesium with foamed polyaniline. *Angew. Chem. Int. Ed.* **55**, 1805–1809 (2016).
37. Shi, M. et al. Long cycle life rechargeable moisture-enabled electricity cell. *Adv. Energy Mater.* **14**, 2303815 (2024).
38. Song, M., Kim, D., Lee, H., Han, H. & Jeon, S. Synergistic effect of a Berlin green framework for highly efficient moisture-electric energy transformation. *Energy Environ. Sci.* **17**, 5421–5428 (2024).
39. Huang, Y. et al. Three-Dimensional Printing of High-Performance Moisture Power Generators. *Adv. Funct. Mater.* **34**, 2308620 (2024).
40. Bubnova, O. et al. Optimization of the thermoelectric figure of merit in the conducting polymer poly(3,4-ethylenedioxythiophene). *Nat. Mater.* **10**, 429–433 (2011).
41. Sun, Y. et al. Organic thermoelectric materials and devices based on p- and n-type poly(metal 1,1,2,2-ethenetetrathiolate)s. *Adv. Mater.* **24**, 932–937 (2012).
42. Han, C.-G. et al. Giant thermopower of ionic gelatin near room temperature. *Science* **368**, 1091–1098 (2020).
43. Qin, Y. et al. Grid-plainification enables medium-temperature PbSe thermoelectrics to cool better than Bi₂Te₃. *Science* **383**, 1204–1209 (2024).
44. Qin, B. et al. Power generation and thermoelectric cooling enabled by momentum and energy multiband alignments. *Science* **373**, 556–561 (2021).
45. Wang, H. et al. Bilayer of polyelectrolyte films for spontaneous power generation in air up to an integrated 1,000 V output. *Nat. Nanotechnol.* **16**, 811–819 (2021).
46. Li, Y. et al. Flexible silicon solar cells with high power-to-weight ratios. *Nature* **626**, 105–110 (2024).
47. Sun, T. et al. Stretchable fabric generates electric power from woven thermoelectric fibers. *Nat. Commun.* **11**, 572 (2020).
48. He, T. et al. Fully printed planar moisture-enabled electric generator arrays for scalable function integration. *Joule* **7**, 935–951 (2023).
49. Kumar, K. S., Pandey, D. & Thomas, J. High Voltage Asymmetric Supercapacitors Developed by Engineering Electrode Work Functions. *ACS Energy Lett.* **6**, 3590–3599 (2021).
50. Ochedowski, O. et al. Effect of contaminations and surface preparation on the work function of single layer MoS₂. *Beilstein J. Nanotechnol.* **5**, 291–297 (2014).

Acknowledgements

This work was supported by the financial support from the National Natural Science Foundation of China No. 22035005, 52090032, 32350362, and 223B2903 (22035005 to L.Q., 52090032 and 32350362 to H.C., 223B2903 to Y.H.). We thank Yongfa Zhu and Jingyi Xu at Department of Chemistry of Tsinghua University for their instruction in UV-vis absorption spectra. We thank Chong Guo at the Analysis Center of Tsinghua University for the help with TOF-SIMS.

Author contributions

L. Q. initiated and guided the research. P. L. designed and performed the experiments. L. Q. and P. L. wrote and revised the manuscript. Y. H., H. W., T. H. and H. C. gave advice on experiments. All authors discussed the results and reviewed the manuscript. L.Q. supervised the entire project.

Competing interests

The authors declare no competing interests.

Additional information

Supplementary information The online version contains supplementary material available at <https://doi.org/10.1038/s41467-025-61913-9>.

Correspondence and requests for materials should be addressed to Liangti Qu.

Peer review information *Nature Communications* thanks the anonymous reviewers for their contribution to the peer review of this work. A peer review file is available.

Reprints and permissions information is available at <http://www.nature.com/reprints>

Publisher's note Springer Nature remains neutral with regard to jurisdictional claims in published maps and institutional affiliations.

Open Access This article is licensed under a Creative Commons Attribution-NonCommercial-NoDerivatives 4.0 International License, which permits any non-commercial use, sharing, distribution and reproduction in any medium or format, as long as you give appropriate credit to the original author(s) and the source, provide a link to the Creative Commons licence, and indicate if you modified the licensed material. You do not have permission under this licence to share adapted material derived from this article or parts of it. The images or other third party material in this article are included in the article's Creative Commons licence, unless indicated otherwise in a credit line to the material. If material is not included in the article's Creative Commons licence and your intended use is not permitted by statutory regulation or exceeds the permitted use, you will need to obtain permission directly from the copyright holder. To view a copy of this licence, visit <http://creativecommons.org/licenses/by-nc-nd/4.0/>.

© The Author(s) 2025